



Influence of Jets on [O iii] Extensions in Green Pea/Bean Galaxies

Downloaded from: <https://research.chalmers.se>, 2026-04-22 14:32 UTC

Citation for the original published paper (version of record):

Bhat, H., Eckart, A., Misquitta, P. et al (2024). Influence of Jets on [O iii] Extensions in Green Pea/Bean Galaxies. *Astrophysical Journal*, 960(2). <http://dx.doi.org/10.3847/1538-4357/ad0f28>

N.B. When citing this work, cite the original published paper.



Influence of Jets on [O III] Extensions in Green Pea/Bean Galaxies

Harshitha K. Bhat^{1,2} , Andreas Eckart^{1,2} , Persis Misquitta¹ , Monica Valencia-S.^{1,3} , Madeleine Yttergren⁴, and Anton Zensus²

¹ I. Physikalisches Institut der Universität zu Köln, Zùlpicher Str. 77, D-50937 Köln, Germany; bhat@ph1.uni-koeln.de

² Max-Planck-Institut für Radioastronomie (MPIfR), Auf dem Hügel 69, D-53121 Bonn, Germany

³ Regional Computer Center (RRZK), Universität zu Köln, Weyertal 121, D-50931 Köln, Germany

⁴ Department of Space, Earth and Environment, Chalmers University of Technology, SE-412 96 Gothenburg, Sweden

Received 2022 December 7; revised 2023 November 8; accepted 2023 November 8; published 2024 January 8

Abstract

We present a study investigating the influence of jets on galaxies exhibiting strong [O III] λ 5007 emission, known as *Green Peas* and *Green Beans*. Our sample comprised 12 nearby sources ($z \sim 0.04$ – 0.1 , six with jets and six without jets) with high [O III] luminosity ($L \sim 10^{40}$ erg s⁻¹), selected from a radio-selected galaxy sample observed with the Sloan Digital Sky Survey and Radio Sky at Twenty-centimeters survey. We perform Large Binocular Telescope–Multi-Object Double Spectrograph long-slit spectroscopy at two position angles for each galaxy: one aligned with the jet direction and another perpendicular to it. By tracing the [O III] emission along these slits, we aimed to assess the extension of the narrow line region and examine the impact of jets. Surprisingly, our analysis revealed no preferred direction for the extension of the [O III] emission, indicating that jets have a limited influence on the extended emission line regions (EELRs). This also suggests the possibility of missed detection of conical-shaped EELRs aligned with the jets, attributable to our slit orientations. Furthermore, we compared the extension of [O II] emission, which traces star-forming regions, with that of [O III]. We observed a significant difference, with [O II] exhibiting a considerably greater extension along the galactic plane. This suggests a stronger association of [O II] emission with stellar processes.

Unified Astronomy Thesaurus concepts: [Extragalactic astronomy \(506\)](#); [Emission line galaxies \(459\)](#); [Active galaxies \(17\)](#)

Supporting material: figure set, machine-readable table

1. Introduction

Extended warm ionized gas, called narrow line regions (NLRs) surrounds radio-loud quasars and is primarily photo-ionized by the hard-ionizing radiation of the active galactic nuclei (AGNs) (Netzer 2015). NLRs can reach up to kiloparsecs and are excited by energetic outflows. In the case of luminous, highly accreting AGNs these outflows can be driven by the radiation pressure (Alexander et al. 2010), whereas in the case of radio-loud sources, they can be initiated by radio cores/jets (Rosario et al. 2010). In some cases, the AGN can ionize gas at larger distances forming extended emission line regions (EELRs) and the strongest narrow emission lines (NELs; e.g., [O III] λ 5007 can trace up to >10 kpc (Stockton & MacKenty 1987; Schmitt et al. 2003; Stockton et al. 2006). EELRs are usually observed in Seyfert 2 galaxies and are characterized by conical or biconical shapes (referred to as ionization cones). The shape of EELRs depends on the luminosity and orientation of the AGN as well as the gas distribution throughout the galaxy (Mulchaey et al. 1996). The gas in the region could be the interstellar medium (ISM) of the host galaxy or gas provided by the mergers or outflows. The ionization cone is often aligned with the radio jet suggesting a strong interaction between ISM and jet, and may even directly enhance their brightness (McCarthy et al. 1987; Wilson & Tsvetanov 1994).

Cardamone et al. (2009) reported a new class of rapidly growing emission line galaxies first noticed by volunteers in the Galaxy Zoo project and called them *Green Peas* (GPs), due to their appearance in *gri* images, where their [O III] lines (that fall in the *r* band) dominate the emission. Among the 112 confirmed GPs, they found 80 star-forming galaxies with high star formation rates (SFRs) and low metallicities, nine Seyfert 1s, 10 Seyfert 2s, and 13 composite galaxies with both AGN and star formation signatures.

Green Beans (GBs) are the galaxies first discovered by Schirmer et al. (2013) with GP colors but much larger and more luminous NLRs than GPs. They exhibit EELRs (20–40 kpc) that are ionized by radio-weak type 2 quasars (Sun et al. 2018). Even though over 98% of type 2 AGNs have radio luminosities larger than 10^{23} W Hz⁻¹, it is less than 50% in the case of GBs (Mullaney et al. 2013), suggesting the significance of radiation pressure in exciting the EELRs. The currently observed AGN activity is much lower than expected from the large angular extent and high [O III] luminosities. This leads to the conclusion that GBs host recently faded AGNs whose activity has declined over timescales less than the light-crossing time of the NLR, resulting in strong light echoes/ionization echoes (Lintott et al. 2009; Knese et al. 2020; Saade et al. 2022). This was further confirmed using X-ray luminosities by Davies et al. (2015), Schirmer et al. (2016).

It is believed that the radio jets can compress the circumnuclear ISM, which leads to enhanced emissions in the NLR. This idea is supported by studies such as those of Schmitt et al. (2003) and Riffel et al. (2006), where a correlation between radio emissions and NLR distributions was observed. However, other studies such as that of Kaiser et al. (2000) have not found this correlation. Barbosa et al. (2009) reported that only a

Table 1
Radio Fluxes and Indices

Source	$S_{1.4 \text{ GHz}}$	$S_{4.85 \text{ GHz}}$	$S_{10.45 \text{ GHz}}$	$\alpha_{(1.4/4.85)}$	$\alpha_{(1.4/10.45)}$	$\log(R)$
L030	0.099	0.023	0.014	-1.176	-0.700	2.61
L048	0.012	0.136	0.008	1.983	-3.700	3.40
L054	0.021	0.009	...	-0.727	...	2.19
L070	0.011	0.006	...	-0.496	...	2.03
L123	0.068	0.026	...	-0.792	...	2.66
L206	0.010	0.006	...	-0.362	...	2.07
J0752/L181	0.050	0.276	0.094	1.373	-1.400	3.72
J0806/H068	0.113	0.077	0.051	-0.312	-0.525	3.13
J1147/H070	0.615	0.223	0.225	-0.816	0.011	3.62
J1352/H074	3.709	1.853	1.067	-0.558	-0.719	4.56
J1440/H059	0.134	0.135	0.114	0.008	-0.219	3.41
J1516/H119	0.756	1.191	1.034	0.366	-0.184	4.35

Note. Radio-loud galaxies ($\log(R) = \log(L_{4.85}/L_O) > 2.4$) are denoted in bold.

subset of their sample shows signatures of this interaction, and they acknowledged the possibility of other mechanisms for NLR outflows such as accretion disk winds. Leipski et al. (2006) found a correlation between radio and NLR sizes but suggested that this could also be due to the influence of the central engine on both parameters. Jarvis et al. (2019) demonstrated a strong relationship between radio emissions and ionized gas kinematics in the 1–25 kpc scales using high-resolution Very Large Array (VLA) observations. Our research aims to build on these findings to examine the influence of jets on NLRs and EELRs in GB/GPs, providing insights into a distinct phase of fading AGNs.

In the sample of Sloan Digital Sky Survey (SDSS) NEL galaxies, which are also detected in the Faint Images of the Radio Sky at Twenty-centimeters (FIRST) radio survey, we chose objects with high [O III] luminosity ($L \sim 10^{40} \text{ erg s}^{-1}$) and equivalent width ($EW \sim 10\text{--}30 \text{ \AA}$). From these, we selected the 12 galaxies (six jetted and six non-jetted) within the redshift range of $0.04 < z < 0.1$, and studied the extension of [O III] and [O II]. We aim to determine the extension of the [O III] emission and the role of radio jets on the EELRs in these sources.

2. Data and Observations

2.1. Source Selection

Vitale et al. (2012) studied a large sample of radio-optical galaxy populations by cross-identifying Sloan Digital Sky Survey (SDSS) galaxies with the FIRST survey. From this sample, a subsample of 119 high-radio flux galaxies (integrated flux density at 1.4 GHz $F_{1.4} > 100 \text{ mJy}$) was collected and observed at the Effelsberg 100 m radio telescope at two frequencies (4.8 and 10.45 GHz) by Vitale et al. (2015). Additionally, Zajaček et al. (2019) observed low-radio flux galaxies ($F_{1.4} > 50 \text{ mJy}$; 298 sources at 4.85 GHz, 90 sources at 10.45 GHz) at Effelsberg and studied the radio spectral index distribution of the combined subsample. The redshifts of the Effelsberg sample were restricted to $0.04 < z < 0.4$ to avoid aperture effects. In Table 1, we present the radio fluxes and the spectral indices calculated between 1.4 GHz (FIRST) and 4.85 GHz (and 10.45 GHz). Here the radio loudness (R) is defined as $L_{4.85}/L_O$, where $L_{4.85}$ is the integrated radio flux density at 4.85 GHz and L_O is the flux density in the SDSS r band in jansky. Sources with $\log(R) > 2.4$ are considered radio-loud, whereas $\log(R) \leq 2.4$ is considered radio quiet (Panessa et al. 2007).

In this SDSS-FIRST-Effelsberg sample, we have encountered objects with characteristically high [O III] luminosity ($L \sim 10^{40} \text{ erg s}^{-1}$) and EW ($EW \sim 10\text{--}30 \text{ \AA}$). We chose 12 such galaxies, six with jets and six without jets, and Figure 1 shows the SDSS r -band images of the galaxies with FIRST contours. The sample galaxies are located within the redshift range of $0.04 < z < 0.1$ (Figure 2) to ensure resolving spatial scales of $< 200 \text{ pc}$ on the source and performed optical long-slit spectroscopy.

2.2. Observations

Optical long-slit spectrometry was carried out at the Large Binocular Telescope (LBT) located at Mt. Graham International Observatory in Arizona, USA. LBT has a binocular design with two circular 8.4 m wide mirrors, making the combined collecting area equivalent to a single circular mirror with a diameter of 11.8 m. Observations were made from 2019 February 9 to 2022 April 27 using the Multi-Object Double Spectrograph (MODS) mounted at the direct Gregorian foci of the mirrors. MODS are a pair of low- to medium-resolution, identical spectrographs covering the UV to near-IR wavelengths (320–1100 nm), with a field-of-view of $6'' \times 6''$. A dichroic placed below each slit splits the beam at a wavelength of 565 nm into red and blue optimized channels.

We used the grating spectroscopy mode with a long $1''$ wide slit, which provides a spectral resolution of about 150 km s^{-1} and spatial resolution of $0''12$.

Each source was observed at two perpendicular slit positions, one along the jet and another perpendicular to it (or along and perpendicular to the galactic plane in the case of non-jetted sources; A and B, respectively, in Figure 1). At each position, we took two exposures, one with the source at the center of the slit and another with $10''$ dithering along the slit direction. Whenever additional telescope time was available, we made multiple exposures at these angles and positions. All the observational details are provided in Table 2.

2.3. Reduction

Observed spectral frames were flat corrected, bias corrected, and combined using the MODS CCD Reduction pipeline (Pogge 2019). Calibrations, background subtraction, and 1D spectra extraction were done using Pyraf scripts adapted from IRAF routines. Along with science observations, wavelength, and flux calibration spectra were also observed. The wavelength was calibrated using Ne, Hg, Kr, Xe, and Ar lamps.

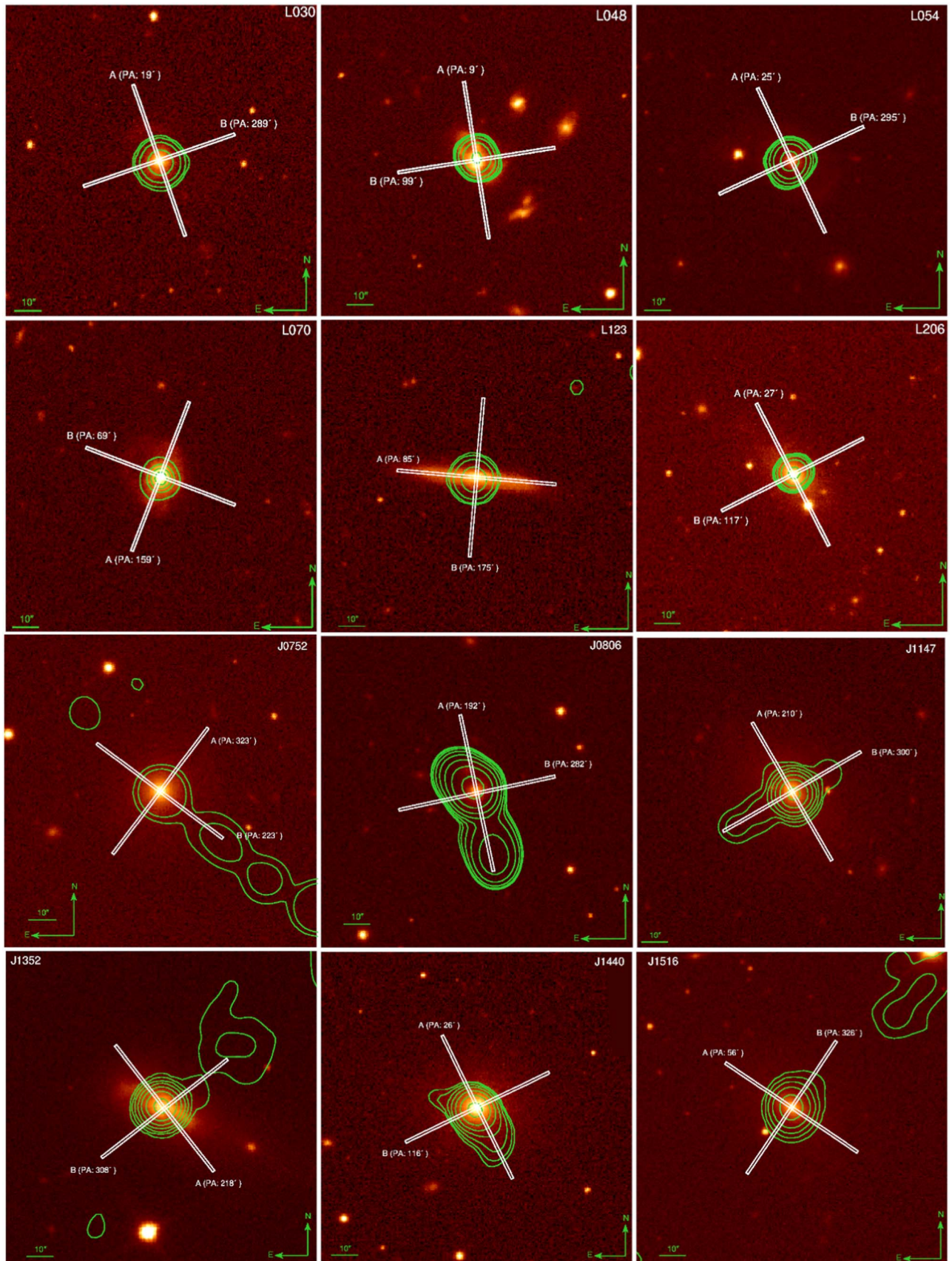


Figure 1. SDSS r -band images of all the galaxies in our sample overplotted with FIRST (1.4 GHz) contours. The contour levels are chosen arbitrarily. Observations were made at two perpendicular slit positions (marked A and B) using a $1''$ slit.

Table 2
Observational Details

Source	Proposal ID	R.A. (α)	Decl. (δ)	Redshift (z)	Date	Exposure time (s)	Position Angle	
							A	B
L030	LBT-2020A-I0002-0	07:57:56.71	39:59:36.13	0.0657	2020-01-20	4800	19	289
	MPIA-2021B-099	2022-02-27/28	4800
L048	MPIA-2020B-099	01:25:16.38	-08:52:25.23	0.0490	2020-10-20	4800	9	99
L054	MPIA-2020B-099	01:37:06.95	-09:08:57.46	0.0697	2020-10-20	6000	25	295
L070	MPIA-2021A-099	11:47:21.61	52:26:58.50	0.0488	2021-04-20	4800	159	69
L123	MPIA-2021B-099	09:50:58.69	37:57:58.87	0.0414	2022-01-27/29	4800	85	175
L206	MPIA-2020B-099	07:52:38.95	18:19:17.75	0.0451	2020-10-20	5400	27	117
J0752/L181	LBT-2018A-I0062-0	07:52:44.19	45:56:57.41	0.0518	2019-02-19	3200	234	144
	MPIA-2021B-099	2022-01-28	4800
J0806/H068	MPIA-2021B-099	08:06:01.51	19:06:14.71	0.0976	2021-11-08	4800	192	282
J1147/H070	LBT-2018A-I0062-0	11:47:22.13	35:01:07.56	0.0631	2019-02-19	3200	210	300
J1352/H074	LBT-2018A-I0062-0	13:52:17.88	31:26:46.49	0.0452	2019-02-09	4800	218	308
J1440/H059	MPIA-2021A-099	14:40:17.98	05:56:34.03	0.0613	2021-05-15/16	4800	26	116
J1516/H119	RDS-2022A-011	15:16:40.21	00:15:01.89	0.0527	2022-04-27	4800	56	326

Note. Project PI Name: Andreas Eckart. Nomenclature by Vitale et al. (2015) and Zajaček et al. (2019) is followed here. Redshifts were estimated using the observed $H\alpha$ line. Whenever a galaxy was observed for more than 1 day, each spectrum was reduced separately and then combined accordingly.

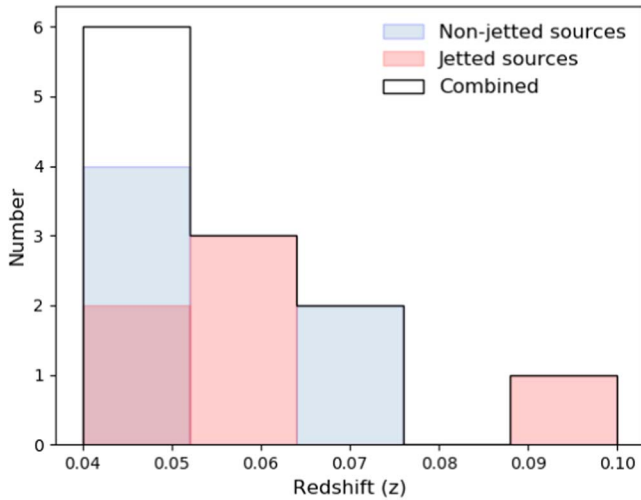


Figure 2. Redshift distribution of the selected GB galaxy sample. The selected GB galaxy sample shows a redshift distribution that mostly falls at the lower end of the range. However, there is no noticeable difference in the distribution between the jetted and non-jetted sets of galaxies.

Spectroscopic standard stars were observed for each observational run and used for flux calibration. All calibration spectra underwent similar reduction processes. Spectra from MODS1 and MODS2 channels and different dithered positions were reduced and then combined accordingly.

3. Spectra

We extract 1D spectra for the central $1''$ aperture from both the position angles and average them to get the spectral lines (Figure 3) at the galactic nuclei. The prominent spectral emission lines are marked in each of the spectra.

We derive flux densities and full width at half maximum (FWHM) by fitting one or more Gaussian functions for each emission line using the Levenberg–Markwardt algorithm, Nonlinear Least-squares Minimization, and Curve-fitting for Python (LMFIT; Markwardt 2009; Newville et al. 2016). The derived flux densities, FWHM, and the wavelength at which the lines were observed are all presented in Table 3. We have

calculated and reported the redshifts in Table 2 using the observed central wavelengths of the $H\alpha$ line (of the narrow component when more than 1 Gaussian was used to fit the broad components of the line) and the formula $z = (\lambda_o - \lambda_l)/\lambda_l$, where λ_o refers to the observed central wavelength, while λ_l is the laboratory wavelength of $H\alpha$, 6562.81 Å. In the following subsections, we give a brief introduction to each galaxy in the sample.

3.1. L030

We cross-identify L030 as B3 0754+401, WISEA J075756.71+395936.1, 2MASX J07575670+3959363, 2MASXi J0757567+395936, and 2MASS J07575671+3959361 using the NASA/IPAC Extragalactic Database.⁵ It has been previously classified as Seyfert 2 by Toba et al. (2014). L030 is one of the non-jetted sources with compact radio emission. The nucleus exhibits several strong emission lines, and the emission in $[O III]\lambda 5007$ is particularly very high. The flux densities and FWHM of the strong emission lines are presented in Table 3. The striking feature of the L030 spectrum is the blueward asymmetries in narrow, high-ionization emission lines, $[O III]\lambda 4959$ and $[O III]\lambda 5007$ as shown in Figure 4. As these forbidden lines trace the low-density ionized gas, the blueshift in the emission line indicates the Doppler effect caused by the gas moving toward us and hence widely used as the outflow signatures in AGNs (Whittle 1985; Leighly & Moore 2004; Crenshaw et al. 2015). By fitting the blue wing with a separate Gaussian, we find that the outflow velocities are 318 and 232 km s^{-1} when derived from $[O III]\lambda 4959$ and $[O III]\lambda 5007$, respectively. L030 also has $[Ne V]\lambda 3427$ and $[N III]\lambda 3869$, which suggests a hard-ionizing spectrum.

3.2. L048

L080 was cross-identified as MCG-02-04-045, WISEA J012516.37-085225.0, 2MASX J01251637-0852250, 2MASS J01251638-0852251, and SDSS J012516.37-085225.2 using

⁵ https://ned.ipac.caltech.edu/byname?objname=B3+0754%2B401&const=67.8&omegam=0.308&omegav=0.692&wmap=4&corr_z=1

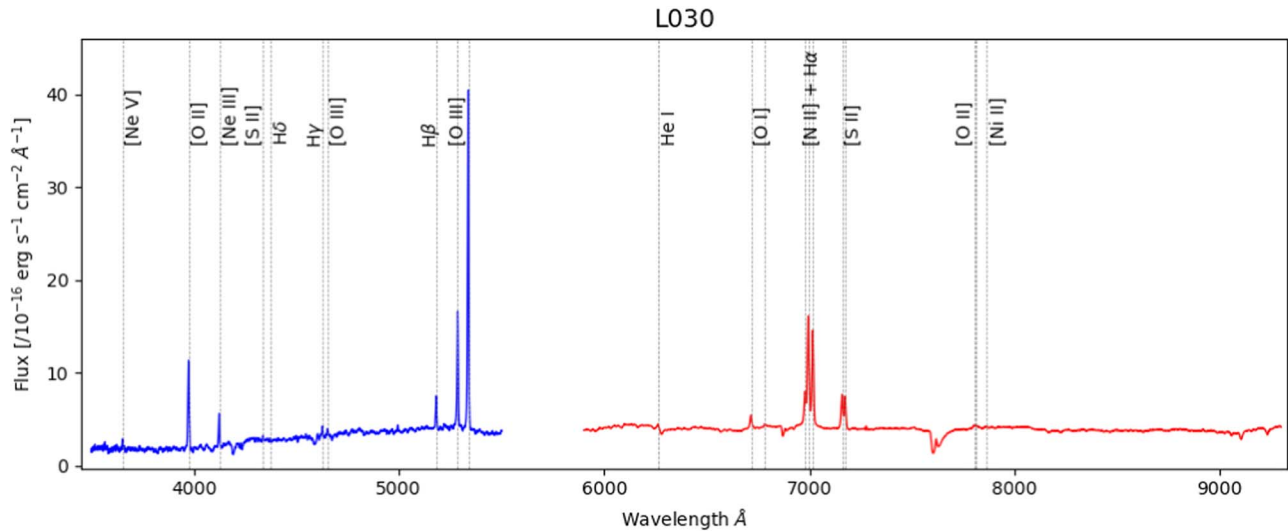


Figure 3. The averaged one-dimensional optical spectrum of the central arcsec of L030. The prominent observed emission lines are marked by dashed lines. The complete figure set for all the galaxies (12 images) is available in the online journal.

(The complete figure set (12 images) is available.)

the NASA/IPAC Extragalactic Database.⁶ It has been classified as a low-power radio galaxy by Lin et al. (2018) and as an AGN by Ge et al. (2012) and Toba et al. (2014). We see several strong emission lines, with broad components in both $H\alpha$ $\lambda 6563$ and $H\beta$ $\lambda 4861$. The blue wing component is present in high-ionization emission lines, $[O III]\lambda 4959$ and $[O III]\lambda 5007$ as well as $[O II]\lambda 3729$ and $[S II]\lambda 6716$. The outflow velocity corresponding to the blue-winged $[O III]\lambda 5007$ line is around 450 km s^{-1} .

3.3. L054

We cross-identify L054 as GIN 086, WISEA J013706.94-090857.3, 2MASX J01370694-0908575, 2MASS J01370694-0908575, and SDSS J013706.94-090857.5 using the NASA/IPAC Extragalactic Database⁷. It has been classified as Seyfert 1 by Oh et al. (2015) and as Seyfert 2 by Toba et al. (2014). Upon analyzing the central spectrum of L054, we observed strong emission lines with broad components in both $H\alpha$ and $H\beta$. Additionally, there are strong outflow signatures in $[Ne III]\lambda 3869$, $[O III]\lambda 4959$, and $[O III]\lambda 5007$, with respective outflow velocities of 214, 111, and 248 km s^{-1} .

3.4. L070

L070 can be cross-identified as MRK 1457, MRK 1456 GROUP NED02, SBS 1144+527B, KUG 1144+527B, and CGCG 268–083 using the NASA/IPAC Extragalactic Database.⁸ L070 is a compact radio galaxy. Its spectrum shows extremely high $[O III]\lambda 5007$ along with $[O III]\lambda 4959$ emission with blue-winged components, indicating outflow velocities reaching up to 200 km s^{-1} . Even though it is classified as Seyfert 2 (Toba et al. 2014), we see broad $H\alpha$ components. It also shows $[Ne V]\lambda 3426$ and $[Ar III]\lambda 7136$, indicating a hard-ionizing spectrum.

3.5. L123

We cross-identified L123 as FGC 0955, RFGC 1643, 2MFGC 07622, WISEA J095058.73+375758.3, and 2MASX J09505867+3757584 using the NASA/IPAC Extragalactic Database.⁹ It is an edge-on galaxy with an elongated morphology. L123 is classified as Seyfert 1 (Toba et al. 2014) and shows a broad $H\alpha$ component. We see that $[O II]\lambda 3729$ is greatly extended along the galactic plane up to 2 kpc from the center, as it can be produced by star formation regions in the galaxy. L123 also shows outflow signatures in $[O III]\lambda 4959, 5007$ with respective outflow velocities of 185 and 135 km s^{-1} .

3.6. L206

We cross-identified L206 as WISEA J075238.95+181917.7, 2MASX J07523897+1819180, 2MASXi J0752389+181918, 2MASS J07523895+1819178, and SDSS J075238.95+181917.7.¹⁰ It is also classified as Seyfert 2 by Toba et al. (2014). It shows several strong narrow lines and has a blue-winged outflow signature in $[O III]\lambda 4959$ line and by fitting a blue-winged component we derive the outflow velocity to be 267 km s^{-1} . It is a compact low-energy radio source and shows extension in $[O III]$ and $[O II]$ along the galactic plane.

3.7. J0752

J0752 can be cross-identified as B3 0749+460A, WISEA J075244.20+455657.4, 2MASX J07524421+4556576, 2MASXi J0752442+455657, and 2MASS J07524421+4556575.¹¹ It is a BL Lac object (D’Abrusco et al. 2019) with high X-ray emission (Cusumano et al. 2010). Its spectrum shows several strong NELs, and is dominated by $[O III]\lambda 5007$ emission in the blue channel and $[N II]\lambda 6583$ emission in the red channel. It

⁶ https://ned.ipac.caltech.edu/byname?objname=MCG+02-04-045&hconst=67.8&omegam=0.308&omegav=0.692&wmap=4&corr_z=1

⁷ https://ned.ipac.caltech.edu/byname?objname=GIN+086&hconst=67.8&omegam=0.308&omegav=0.692&wmap=4&corr_z=1

⁸ https://ned.ipac.caltech.edu/byname?objname=MRK+1457&hconst=67.8&omegam=0.308&omegav=0.692&wmap=4&corr_z=1

⁹ https://ned.ipac.caltech.edu/byname?objname=FGC+0955&hconst=67.8&omegam=0.308&omegav=0.692&wmap=4&corr_z=1

¹⁰ https://ned.ipac.caltech.edu/byname?objname=WISEA+J075238.95%2B181917.7&hconst=67.8&omegam=0.308&omegav=0.692&wmap=4&corr_z=1

¹¹ https://ned.ipac.caltech.edu/byname?objname=B3+0749%2B460A&hconst=67.8&omegam=0.308&omegav=0.692&wmap=4&corr_z=1

Table 3
Central Emission Lines of L030

Emission line	Observed Wavelength (λ_o) (Å)	$\Delta\lambda_o$ (Å)	Flux (F) (10^{-16} erg s^{-1} cm^{-2})	ΔF (10^{-16} erg s^{-1} cm^{-2})	FWHM ($km s^{-1}$)	$\Delta FWHM$ ($km s^{-1}$)
[Ne V] λ 3426	3652.7	0.19	6.31	0.41	466.0	34.0
[O II] λ 3729	3973.09	0.02	66.35	0.44	489.0	4.0
[Ne III] λ 3869	4124.31	0.2	8.6	3.97	276.0	44.0
H γ λ 4340	4626.36	0.25	5.52	0.5	340.0	36.0
[O III] λ 4363	4651.22	0.39	4.93	0.57	427.0	56.0
H β λ 4861	5181.62	0.04	20.32	0.32	321.0	6.0
[O III] λ 4959 _{blue}	5280.64	0.45	12.55	1.46	401.0	85.0
[O III] λ 4959	5286.25	0.05	68.14	1.69	303.0	4.0
[O III] λ 5007 _{blue}	5333.3	0.96	43.21	13.12	397.0	90.0
[O III] λ 5007	5337.43	0.06	184.02	13.01	291.0	4.0
He I λ 5876	6260.77	0.74	2.65	0.59	306.0	79.0
[O I] λ 6300	6714.75	0.26	13.57	0.72	423.0	26.0
[N II] λ 6548	6978.25	0.22	19.97	2.79	333.0	26.0
H α λ 6563	6994.16	0.05	78.76	3.45	329.0	7.0
H α λ 6563 _{broad1}	6992.25	1.27	42.96	8.77	1102.0	157.0
H α λ 6563 _{broad2}	6994.23	1.46	70.42	6.8	3129.0	237.0
[N II] λ 6583	7016.22	0.04	87.69	1.34	368.0	4.0
[S II] λ 6716	7158.18	0.11	37.3	0.85	412.0	11.0
[S II] λ 6731	7173.37	0.11	32.35	0.81	365.0	11.0
[O II] λ 7320	7801.61	0.37	1.34	0.28	262.0	40.0
[O II] λ 7331	7811.62	0.64	8.7	0.46	13.0	0.0
[Ni II] λ 7378	7861.51	0.45	2.79	0.2	514.0	39.0

Note. Tables for all 12 galaxies are published in its entirety in the machine-readable format. An example of L030 is shown here for guidance regarding its form and content.

(This table is available in its entirety in machine-readable form.)

has a radio jet in one direction extending up to $3'$. The outflow signatures in [O III] λ 4959,5007 indicate respective velocities of 225 and 94 $km s^{-1}$.

3.8. J0806

We cross-identified J0806 as WISEA J080601.54+190614.6, 2MASX J08060148+1906142, 2MASS J08060153+1906148, SDSS J080601.51+190614.7, and SDSS J080601.52+190614.7.¹² It is a Seyfert 2 (Toba et al. 2014) with compact high energy radio emission. Its spectrum is dominated by [O III] λ 5007 emission, and has weaker H α and H β emission but no outflow signatures.

3.9. J1147

J1147 was cross-identified as CGCG 186-048, CGCG 1144.7+3518, B2 1144+35B, 2MASX J11472209+3501071, and 2MASXi J1147220+350107.¹³ It has been classified as a BL Lac object by D'Abrusco et al. (2019), as Seyfert 1 by Oh et al. (2015), and as Seyfert 2 by Toba et al. (2014). It is a compact radio source with relatively smaller jets extending up to $30''$ on either side. Its spectrum is dominated by extremely high [O III] λ 5007 emission with an outflow signature whose velocities reach up to 178 $km s^{-1}$. It is known to have high X-ray emission (Malizia et al. 2016), which confirms the presence of AGN.

¹² https://ned.ipac.caltech.edu/byname?objname=WISEA+J080601.54%2B190614.6&hconst=67.8&omegam=0.308&omegav=0.692&wmap=4&corr_z=1

¹³ https://ned.ipac.caltech.edu/byname?objname=CGCG+186-048&hconst=67.8&omegam=0.308&omegav=0.692&wmap=4&corr_z=1

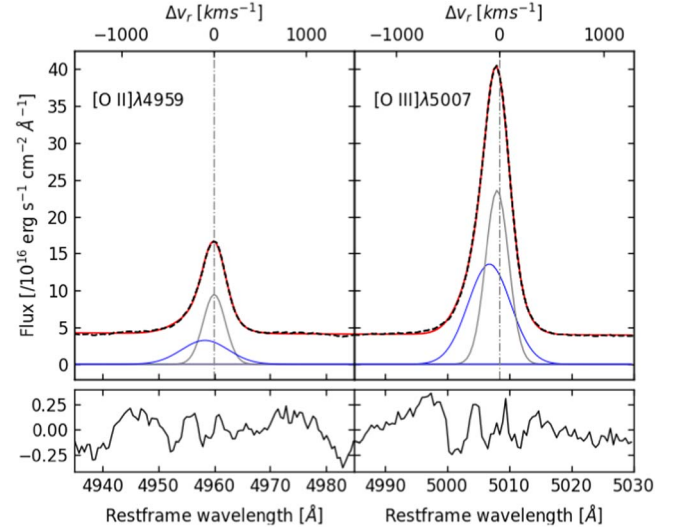


Figure 4. [O III] λ 4959,5007 region from the central $1''$ spectrum of L030. Black-dashed line: continuum with emission lines around [O III] λ 4959,5007. Grey solid line: Gaussian fit at the line center. Blue solid line: Gaussian fit to account for the blue wing in the emission line. Red solid line: model spectra produced by combining both the Gaussians at each emission line. The lower panel shows the observed minus model residuals.

3.10. J1352

We cross-identified J1352 as UGC 08782, VV 369, CGCG 162-021, CGCG 1350.0+3142, and MCG +05-33-012.¹⁴ It has been classified as a BL Lac object by D'Abrusco et al. (2019).

¹⁴ https://ned.ipac.caltech.edu/byname?objname=UGC+08782&hconst=67.8&omegam=0.308&omegav=0.692&wmap=4&corr_z=1

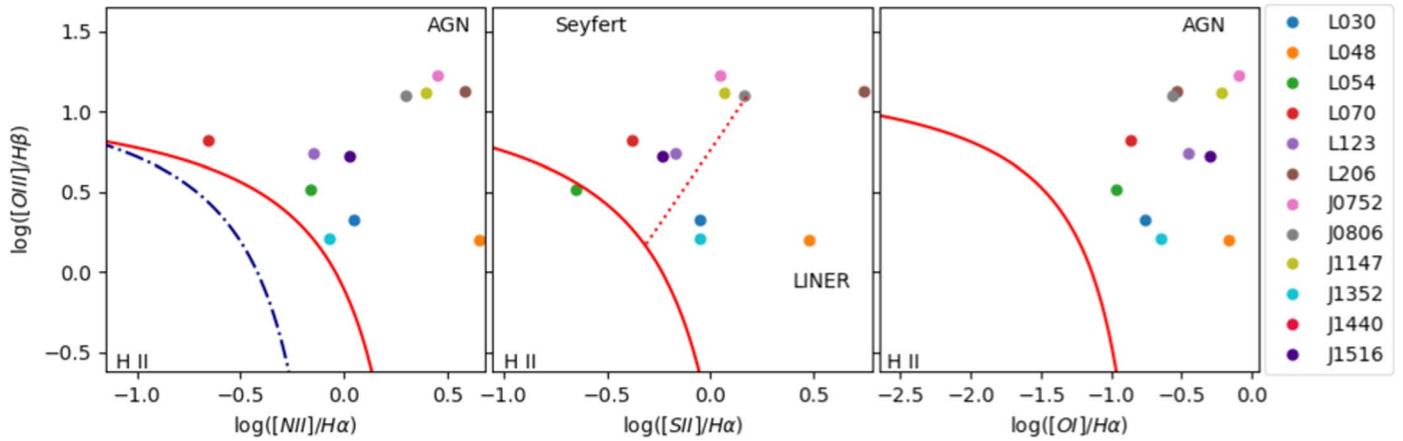


Figure 5. BPT diagram using the flux ratios of central 1". All the galaxies fall at the higher end of $\log([\text{O III}]/\text{H}\beta)$ ratio, indicating the presence of AGN.

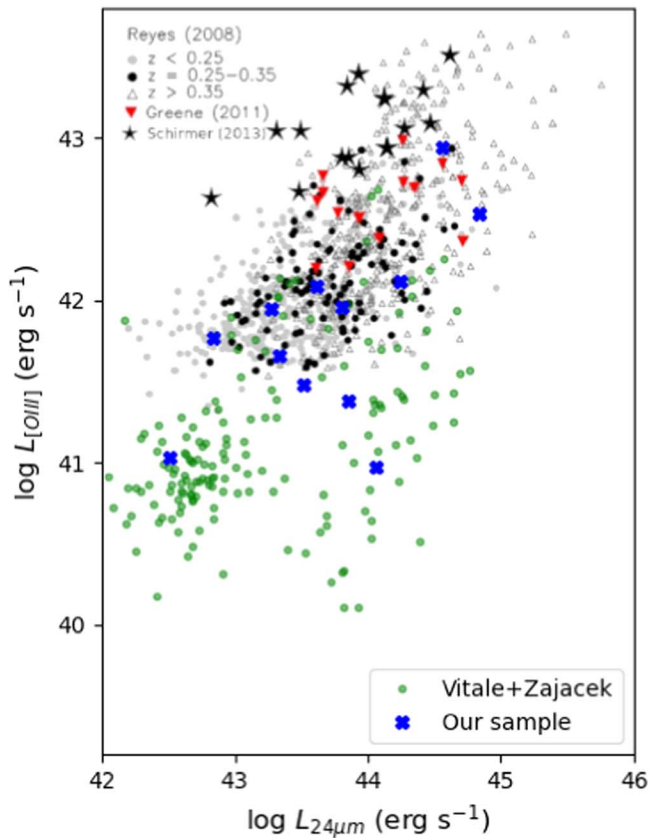


Figure 6. WISE 24 μm vs. $[\text{O III}]\lambda 5007$ luminosities from Schirmer et al. (2013) overplotted with Vitale et al. (2015) and Zajaček et al. (2019) sources in the range of $0.04 < z < 0.1$. Due to the difference in selection processes, VZ sources exhibit both lower $L_{[\text{O III}]}$ and lower $L_{24\mu\text{m}}$ values. However, among these radio-selected VZ sources, our GB sample (blue crosses) stands out with higher $[\text{O III}]$ luminosities.

Its 1D spectrum shows several emission lines including a broad $\text{H}\alpha$ line. Interestingly, $[\text{O II}]\lambda 3729$ emission dominates the blue channel, indicating softer ionizing spectra. Blue-winged components are evident in $[\text{O II}]\lambda 3729$, $[\text{O III}]\lambda 4959$, $[\text{O III}]\lambda 5007$, and $[\text{S II}]\lambda 6716$ and indicate strong outflows up to 278 km s^{-1} in the central regions of the galaxy. J1352 also has X-ray emission (Ueda et al. 2005). FIRST radio contours show highly extended jets in both directions; however, the one pointing northwest (Figure 1) is much brighter.

3.11. J1440

We cross-identified J1440 as 2MASX J14401795+0556341, GALEXASC J144017.93+055633.9, GALEXMSC J144018.03+055634.6, SPIDER J220.07493+05.94279, and SDSS J144017.98+055634.0.¹⁵ It has been classified as Seyfert 2 by Toba et al. (2014). We see several NELs; however, $\text{H}\alpha$ is very weak and $\text{H}\beta$ could not be detected. We also see a blue-winged outflow signature in $[\text{O III}]\lambda 5007$ with an outflow velocity of around 590 km s^{-1} . Radio contours show a jet-like morphology on one side of the galaxy.

3.12. J1516

J1516 was cross-identified with several other objects such as CGCG 021-063, CGCG 1514.1+0025, 4C +00.56, PKS 1514+00, and WISEA J151640.21+001501.9.¹⁶ According to Oh et al. (2015), it is classified as a Seyfert 1 object, while D'Abrusco et al. (2019) classify it as a BL Lac object. J1516 also shows X-ray emission (Nisbet & Best 2016). The one-dimensional spectrum of central 1" shows strong emission lines, including $[\text{O III}]\lambda 4959, 500$ and the $[\text{N II}]\lambda 6548, 6583 + \text{H}\alpha \lambda 6563$ complex, but no noticeable outflow signatures in the $[\text{O III}]\lambda 4959, 5007$ lines. The spectrum also reveals a stellar continuum. The FIRST images (green contours in Figure 1) show the jets in both directions extending over 4'.

4. Results

4.1. Diagnostic Diagrams

Unlike BLRs, NLRs do not directly indicate nuclear activity. As our spectra consist of dominant NELs, we use the diagnostic diagrams devised by Baldwin et al. (1981) to categorize our sources based on their primary ionizing source. The Baldwin–Phillips–Terlevich (BPT) diagram along with the diagnostic diagrams introduced by Veilleux & Osterbrock (1987), use emission line ratios ($[\text{O III}]/\text{H}\beta$, $[\text{N II}]/\text{H}\alpha$, $[\text{S II}]/\text{H}\alpha$, and $[\text{O I}]/\text{H}\alpha$) to classify galaxies into starburst galaxies or active galaxies. Kewley et al. (2001) proposed theoretical models to predict the maximum star formation contribution, represented by red solid lines in Figure 5 and Kauffmann et al. (2003)

¹⁵ https://ned.ipac.caltech.edu/byname?objname=2MASX+J14401795%2B0556341&hconst=67.8&omegam=0.308&omegav=0.692&wmap=4&corr_z=1

¹⁶ https://ned.ipac.caltech.edu/byname?objname=CGCG%20021-063&hconst=67.8&omegam=0.308&omegav=0.692&wmap=4&corr_z=1

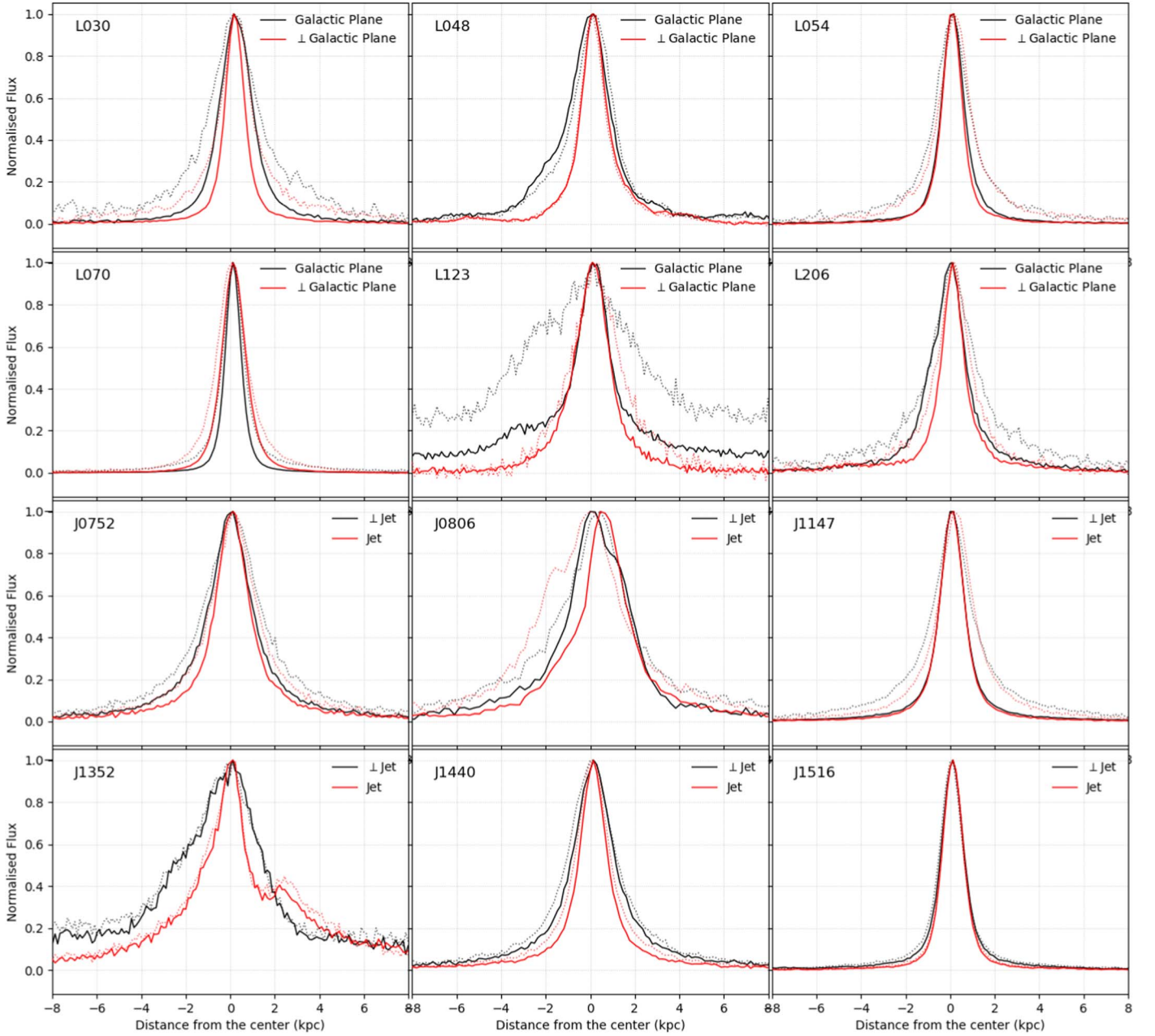


Figure 7. Extension of $[\text{O III}]\lambda 5007$: Normalized flux is plotted as a function of distance from the center of the galaxy. The top six panels correspond to non-jetted compact radio sources and the bottom six panels correspond to the jetted source. The black solid line represents $[\text{O III}]\lambda 5007$ flux along the galactic plane (or perpendicular to the jet for jetted sources), whereas the black-dotted line represents the continuum flux in the same direction. Similarly, the red solid line represents $[\text{O III}]\lambda 5007$ in the direction perpendicular to the galactic plane (or along the jet for the jetted sources) and the red-dotted line represents the continuum flux from the same 2D spectrum.

empirically moved this line (blue-dotted-dashed line) based on extensive observational data. The objects that fall between the two lines are considered transition objects, with both ongoing star formation and AGN. Figure 5 shows that all the sources in our sample have AGNs as their dominant ionizing source and some may even be classified as low-ionization nuclear emission line regions (LINERs).

4.2. Mid-IR versus $[\text{O III}]\lambda 5007$ Luminosities

Low-luminosity AGNs are believed to represent the initial or final stages of the galaxies' active phases. Thermal emission from the warm dusty torus is strongest in the mid-IR (MIR), and the observed MIR luminosities represent the reprocessed

UV/X-ray radiation from the dusty clouds inside the torus. MIR emission also correlates with the X-ray brightness over a wide range of luminosities and hence can be used as a proxy for AGN activity (Lutz et al. 2004; Horst et al. 2009; Asmus et al. 2011).

Schirmer et al. (2013) compared the MIR- $[\text{O III}]$ relation of a set of GBs with a larger sample of type 2 galaxies from Reyes et al. (2008) and Greene et al. (2011). They plot the Wide-field Infrared Survey Explorer (WISE) luminosities at $24\ \mu\text{m}$ (W4 filter, as it is not affected by dust absorption) against $[\text{O III}]\lambda 5007$ luminosities and conclude that the $24\ \mu\text{m}$ luminosities of GBs are in the same range as other obscured type 2 galaxies; however, their $[\text{O III}]$ emission was 5–50 times

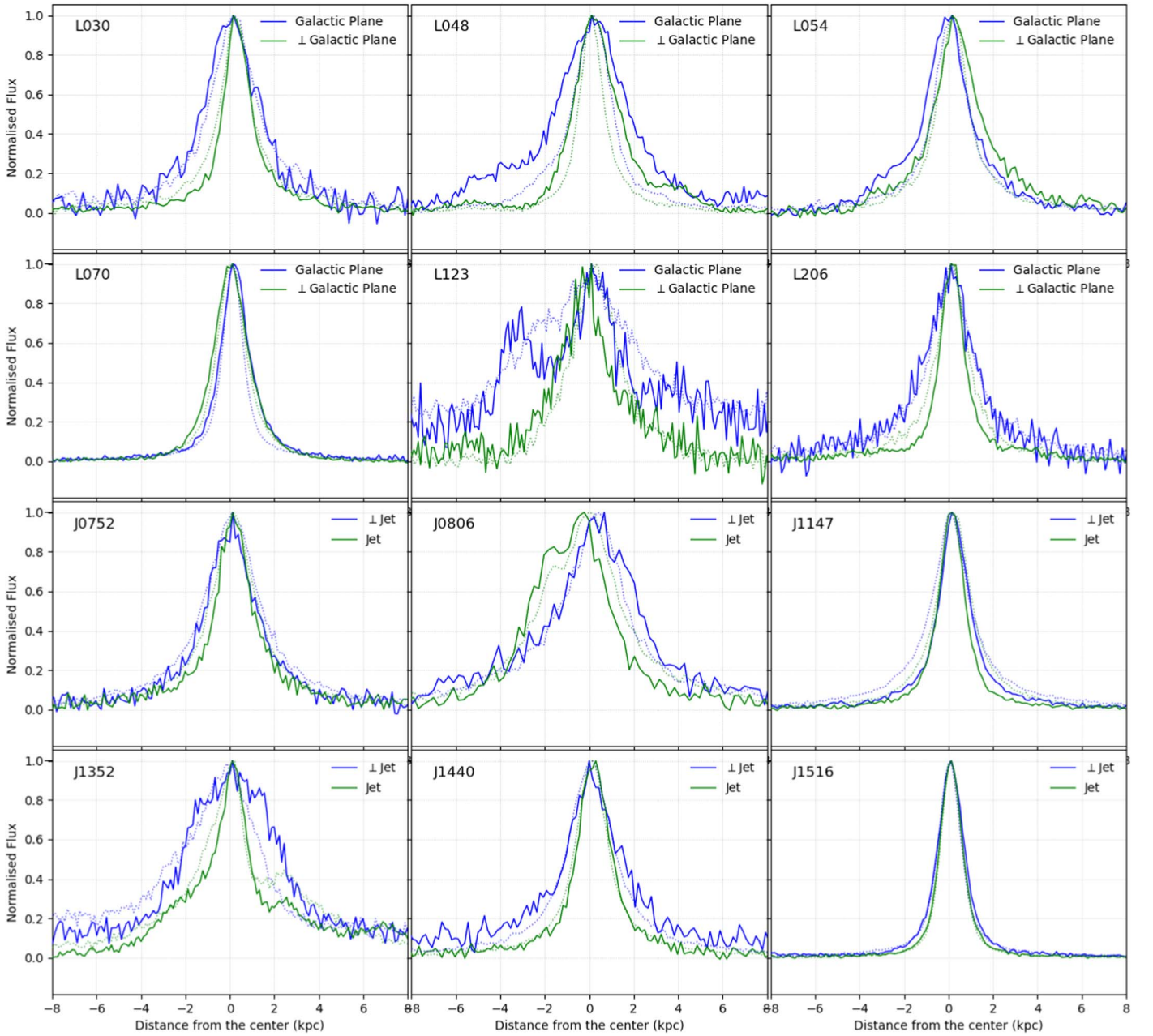


Figure 8. Extension of $[\text{O III}]\lambda 3729$: Normalized flux is plotted as a function of distance from the center of the galaxy. The top six panels correspond to non-jetted compact radio sources and the bottom six panels correspond to the jetted source. The blue solid line represents $[\text{O III}]\lambda 3729$ flux along the galactic plane (or perpendicular to the jet for jetted sources), whereas the blue-dotted line represents the continuum flux in the same direction. Similarly, the green solid line represents $[\text{O III}]\lambda 3729$ in the direction perpendicular to the galactic plane (or along the jet for the jetted sources) and the green dotted line represents the continuum flux from the same 2D spectrum.

greater. This could be explained by the light echo scenario where the NLR is reflecting an earlier active state of AGN, which has declined significantly in less than the light-crossing time.

We overplot MIR and $[\text{O III}]$ luminosities of the Vitale et al. (2015) and Zajaček et al. (2019) sources over the Schirmer et al. (2013) plot in Figure 6. It is to be noted that the redshift range of radio-selected galaxies was constrained to $0.04 < z < 0.1$ to match the galaxy sample considered in this paper. We see a general trend of lower $[\text{O III}]$ luminosities in radio-selected galaxies, compared to the type 2 galaxies covered in Reyes et al. (2008) and Greene et al. (2011). However, among the radio-selected galaxies, our GB sample stands out with

higher $[\text{O III}]$ luminosities even though the two are indistinguishable in the MIR.

When compared with the findings in Schirmer et al. (2013), we find that the radio selection does not particularly increase the number of sources with strong $[\text{O III}]$ line emission. Only two out of 12 sources in our sample fell within the $[\text{O III}]$ luminosity range in Schirmer et al. (2013).

Strong radio emission can indicate recent activity (by feeding the central black hole) or enhanced high-mass star formation. We find that despite stronger nonthermal radio emission, there was no significant decline in line emission during bulge crossing timescales. This may be obvious in jetted

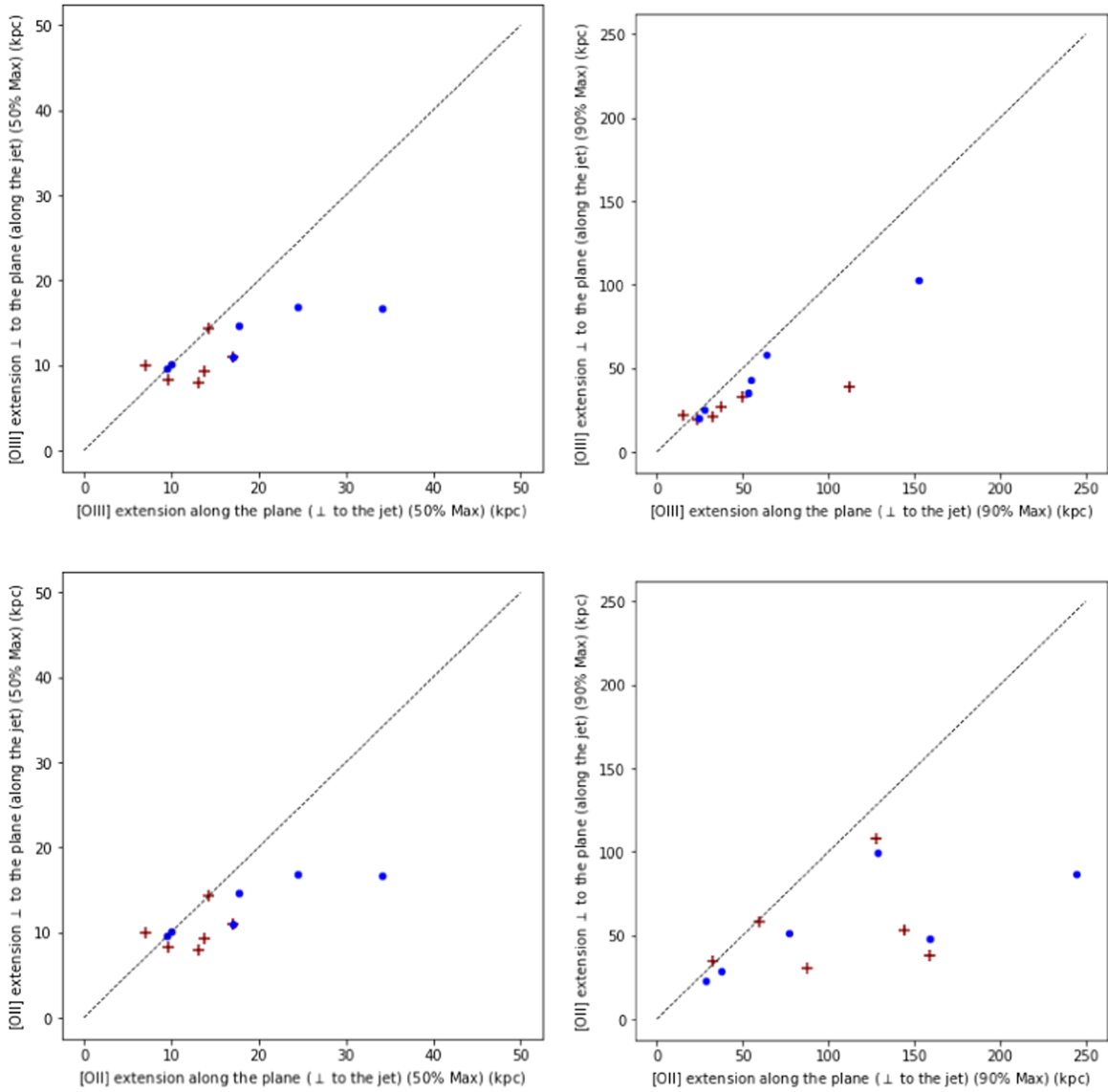


Figure 9. We conducted a comparison of the extensions of [O III] and [O II] plots in parallel and perpendicular planes. The non-jetted sources are marked with maroon + signs, while jetted sources are marked with blue dots. The dashed black line represents the point where the widths along both directions would be equal. In all the figures except the bottom right figure ([O II] widths at 90% max), the plot points cluster around the dashed line, indicating no preferential direction. However, in the bottom right figure, we observed that the extension widths along the galactic plane were significantly more compared to the perpendicular plane. The K-S test confirmed this finding.

sources, as the presence of a jet with expansion speeds less than the speed of light suggests prolonged ongoing quasi-continuous activity. However, in non-jetted sources, such an argument is less obvious but indicates nuclear activity on timescales that exceed bulge crossing timescales.

4.3. Extended Emission

To examine the relationship between NELs and the distance from the galactic center, we made a cut across the 2D spectrum at the line position. Our cut was carefully chosen to encompass the velocity dispersion of the galaxy, while ensuring no overlap from neighboring lines. The resulting plot in Figure 7 illustrates the normalized flux of [O III] λ 5007 across the galaxy, alongside the continuum fluxes. This representation allows for a fair comparison of line extensions along and perpendicular to the radio jets. A similar plot for [O II] λ 3729 is presented in Figure 8.

To investigate whether there is a preferred direction for the extended [O III] emission, we measured the full widths at 50% and 90% of the maximum flux in both directions, as shown in Figure 9. We conducted a two Kolmogorov–Smirnov (K-S) test between the distributions in either direction ((i). 50% of maximum flux— \parallel plane versus \perp plane; (ii) 90% of maximum flux— \parallel plane versus \perp plane) to compare the extended widths along the parallel and perpendicular planes. The resulting p -values of 0.249 and 0.518, respectively, indicate no significant systematic difference between the samples, suggesting the absence of a preferred direction for the [O III] emission.

In contrast, when comparing the extended [O II] emission, we observed a distinct pattern. The p -value of approximately 0.034 obtained from FWHM along the parallel plane versus the perpendicular plane suggests two different distributions between the samples. Specifically, [O II] exhibits systematic extensions primarily along the galactic plane. This behavior can

Table 4The p -values from the K-S-test for Comparison between Different Categories of Extension Widths

	[O III]	[O II]
FWHM (entire sample)— plane versus \perp plane	0.249	0.034
90% of maxima (entire sample)— plane versus \perp plane	0.518	0.100
FWHM plane—non-jetted versus jetted	0.139	0.893
FWHM \perp plane—non-jetted versus jetted	0.441	0.441
FWHM plane /FWHM \perp plane—non-jetted versus jetted	1.000	0.893

be attributed to the lower ionizing potential of [O II] and its production by stellar photons.

To estimate the impact of jet presence on the observed extensions, we conducted separate tests for jetted and non-jetted sources. The corresponding p -values are presented in Table 4, indicating no significant difference in the extensions between the two groups. However, it is worth noting that the conical shape of the ionized NLR implies a potential misalignment between the slit position and the EELR associated with the jets. Therefore, the observed lack of extended [O III] emission in those regions could be attributed to this misalignment.

In summary, our study examined the extensions of NELs about the galactic center. The analysis revealed no preferred direction for the extended [O III] emission, while demonstrating the systematic extensions of [O II] predominantly along the galactic plane. Furthermore, the lack of significant differences in extensions between jetted and non-jetted sources suggests the need for careful consideration of the alignment between the slit position and the EELR in future studies.

5. Summary

In this study, we focused on galaxies exhibiting strong [O III] $\lambda 5007$ emission, which has been associated with extreme star formation and/or AGNs in the literature. These galaxies, often referred to as GPs and GBs, display a prominent appearance in gri images, due to the dominance of their [O III] lines (which fall in the r band). From a larger radio-selected galaxy sample observed with SDSS-FIRST, we selected 12 nearby sources (with redshifts approximately ranging from 0.04–0.1), characterized by high [O III] luminosity ($L \sim 10^{40}$ erg s $^{-1}$).

To investigate the potential impact of jets on the EELRs, we conducted LBT-MODS long-slit spectroscopy at two different position angles for each selected galaxy. One slit was aligned along the direction of the jet, while the other was oriented perpendicular to it. By tracing the [O III] emission along both slit positions, we aimed to estimate the extension of the NLR.

Our analysis revealed that no preferential direction exists for the extension of the [O III] emission, suggesting that the presence of jets does not significantly affect the EELRs. This finding implies that if the EELRs are conical in shape with their axes aligned with the jets, we may have missed their detection by placing the slits parallel or perpendicular to the jet directions.

Furthermore, we also plotted the extension of [O II] emission, which traces the star-forming regions within the galaxy. Interestingly, we observed that [O II] exhibits a much greater extension along the galactic plane compared to [O III]. This disparity could be due to the lower ionization potential of [O II] and its association with stellar processes.

In summary, our study of high [O III]-emitting galaxies selected from a radio-selected sample demonstrated no preferential direction for the extension of [O III] emission, suggesting a limited impact of jets on the EELRs. We highlighted the possibility of missing conical-shaped EELRs aligned with the jets by using slits along or perpendicular to the jet directions. Moreover, the significant extension of [O II] emission along the galactic plane emphasized its association with star-forming regions within the galaxies.

Acknowledgments

We would like to thank the reviewer for their constructive suggestions and feedback that helped us significantly improve the quality of this manuscript. This work was supported in part by SFB 956—Conditions and Impact of Star Formation. We thank the Collaborative Research Centre 956, sub-project A02, funded by the Deutsche Forschungsgemeinschaft (DFG)—project ID 184018867. H.B. was a member of the International Max Planck Research School for Astronomy and Astrophysics at the Universities of Bonn and Cologne and has received financial support for this research from IMPRS.

ORCID iDs

Harshitha K. Bhat  <https://orcid.org/0000-0002-4408-0650>
 Andreas Eckart  <https://orcid.org/0000-0001-6049-3132>
 Persis Misquitta  <https://orcid.org/0000-0003-3168-9448>
 Monica Valencia-S.  <https://orcid.org/0000-0003-3430-2683>
 Anton Zensus  <https://orcid.org/0000-0001-7470-3321>

References

- Alexander, D. M., Swinbank, A. M., Smail, I., McDermaid, R., & Nesvadba, N. P. H. 2010, *MNRAS*, **402**, 2211
- Asmus, D., Gandhi, P., Smette, A., Hönig, S. F., & Duschl, W. J. 2011, *A&A*, **536**, A36
- Baldwin, J. A., Phillips, M. M., & Terlevich, R. 1981, *PASP*, **93**, 5
- Barbosa, F. K. B., Storchi-Bergmann, T., Cid Fernandes, R., Winge, C., & Schmitt, H. 2009, *MNRAS*, **396**, 2
- Cardamone, C., Schawinski, K., Sarzi, M., et al. 2009, *MNRAS*, **399**, 1191
- Crenshaw, D. M., Fischer, T. C., Kraemer, S. B., & Schmitt, H. R. 2015, *ApJ*, **799**, 83
- Cusumano, G., La Parola, V., Segreto, A., et al. 2010, *A&A*, **524**, A64
- D’Abrusco, R., Álvarez Crespo, N., Massaro, F., et al. 2019, *ApJS*, **242**, 4
- Davies, R. L., Schirmer, M., & Turner, J. E. H. 2015, *MNRAS*, **449**, 1731
- Ge, J.-Q., Hu, C., Wang, J.-M., Bai, J.-M., & Zhang, S. 2012, *ApJS*, **201**, 31
- Greene, J. E., Zakamska, N. L., Ho, L. C., & Barth, A. J. 2011, *ApJ*, **732**, 9
- Horst, H., Duschl, W. J., Gandhi, P., & Smette, A. 2009, *A&A*, **495**, 137
- Jarvis, M. E., Harrison, C. M., Thomson, A. P., et al. 2019, *MNRAS*, **485**, 2710
- Kaiser, M. E., Bradley, L. D. I., Hutchings, J. B., et al. 2000, *ApJ*, **528**, 260
- Kauffmann, G., Heckman, T. M., Tremonti, C., et al. 2003, *MNRAS*, **346**, 1055
- Kewley, L. J., Dopita, M. A., Sutherland, R. S., Heisler, C. A., & Trevena, J. 2001, *ApJ*, **556**, 121
- Knese, E. D., Keel, W. C., Knese, G., et al. 2020, *MNRAS*, **496**, 1035
- Leighly, K. M., & Moore, J. R. 2004, *ApJ*, **611**, 107
- Leipski, C., Falcke, H., Bennert, N., & Hüttemeister, S. 2006, *A&A*, **455**, 161
- Lin, Y.-T., Huang, H.-J., & Chen, Y.-C. 2018, *AJ*, **155**, 188
- Lintott, C. J., Schawinski, K., Keel, W., et al. 2009, *MNRAS*, **399**, 129
- Lutz, D., Maiolino, R., Spoon, H. W. W., & Moorwood, A. F. M. 2004, *A&A*, **418**, 465
- Malizia, A., Landi, R., Molina, M., et al. 2016, *MNRAS*, **460**, 19
- Markwardt, C. B. 2009, in ASP Conf. Ser. 411, *Astronomical Data Analysis Software and Systems XVIII*, ed. D. A. Bohlender, D. Durand, & P. Dowler (San Francisco, CA: ASP), 251
- McCarthy, P. J., van Breugel, W., Spinrad, H., & Djorgovski, S. 1987, *ApJL*, **321**, L29
- Mulchaey, J. S., Wilson, A. S., & Tsvetanov, Z. 1996, *ApJS*, **102**, 309
- Mullaney, J. R., Alexander, D. M., Fine, S., et al. 2013, *MNRAS*, **433**, 622

- Netzer, H. 2015, *ARA&A*, **53**, 365
- Newville, M., Stensitzki, T., Allen, D. B., et al., 2016 Lmfit: Non-Linear Least-Square Minimization and Curve-Fitting for Python, Astrophysics Source Code Library, ascl:[1606.014](#)
- Nisbet, D. M., & Best, P. N. 2016, *MNRAS*, **455**, 2551
- Oh, K., Yi, S. K., Schawinski, K., et al. 2015, *ApJS*, **219**, 1
- Panessa, F., Barcons, X., Bassani, L., et al. 2007, *A&A*, **467**, 519
- Pogge, R., 2019 [rwpogge/modsCCDRed v2.0](#), Zenodo, doi:[10.5281/zenodo.2550741](#)
- Reyes, R., Zakamska, N. L., Strauss, M. A., et al. 2008, *AJ*, **136**, 2373
- Riffel, R. A., Storchi-Bergmann, T., Winge, C., & Barbosa, F. K. B. 2006, *MNRAS*, **373**, 2
- Rosario, D. J., Shields, G. A., Taylor, G. B., Salviander, S., & Smith, K. L. 2010, *ApJ*, **716**, 131
- Saade, M. L., Brightman, M., Stern, D., Malkan, M. A., & García, J. A. 2022, *ApJ*, **936**, 162
- Schirmer, M., Diaz, R., Holmberg, K., Levenson, N. A., & Winge, C. 2013, *ApJ*, **763**, 60
- Schirmer, M., Malhotra, S., Levenson, N. A., et al. 2016, *MNRAS*, **463**, 1554
- Schmitt, H. R., Donley, J. L., Antonucci, R. R. J., et al. 2003, *ApJ*, **597**, 768
- Stockton, A., Fu, H., & Canalizo, G. 2006, *NewAR*, **50**, 694
- Stockton, A., & MacKenty, J. W. 1987, *ApJ*, **316**, 584
- Sun, A.-L., Greene, J. E., Zakamska, N. L., et al. 2018, *MNRAS*, **480**, 2302
- Toba, Y., Oyabu, S., Matsuhara, H., et al. 2014, *ApJ*, **788**, 45
- Ueda, Y., Ishisaki, Y., Takahashi, T., Makishima, K., & Ohashi, T. 2005, *ApJS*, **161**, 185
- Veilleux, S., & Osterbrock, D. E. 1987, *ApJS*, **63**, 295
- Vitale, M., Fuhrmann, L., García-Marín, M., et al. 2015, *A&A*, **573**, A93
- Vitale, M., Zuther, J., García-Marín, M., et al. 2012, *A&A*, **546**, A17
- Whittle, M. 1985, *MNRAS*, **213**, 1
- Wilson, A. S., & Tsvetanov, Z. I. 1994, *AJ*, **107**, 1227
- Zajaček, M., Busch, G., Valencia-S., M., et al. 2019, *A&A*, **630**, A83